Title

Excited-State Dynamics during Primary C—I Homolysis in Acetyl Iodide Revealed by Ultrafast Core-Level Spectroscopy

Authors

Troß, Jan

Carter-Fenk, Kevin

Cole-Filipiak, Neil C

et al.

Peer reviewed

Excited-State Dynamics during Primary C–I Homolysis in Acetyl Iodide Revealed by Ultrafast Core-Level Spectroscopy

Jan Troß[||],

Combustion Research Facility, Sandia National Laboratories, Livermore, California 94550, United States;

Kevin Carter-Fenk[||],

Kenneth S. Pitzer Center for Theoretical Chemistry, Department of Chemistry, University of California, Berkeley, California 94720, United States;

Neil C. Cole-Filipiak,

Combustion Research Facility, Sandia National Laboratories, Livermore, California 94550, United States;

Paul Schrader,

Combustion Research Facility, Sandia National Laboratories, Livermore, California 94550, United States

Mi'Kayla Word,

Combustion Research Facility, Sandia National Laboratories, Livermore, California 94550, United States

Laura M. McCaslin,

Combustion Research Facility, Sandia National Laboratories, Livermore, California 94550, United States;

Martin Head-Gordon,

Corresponding Authors: Kevin Carter-Fenk – Kenneth S. Pitzer Center for Theoretical Chemistry, Department of Chemistry, University of California, Berkeley, California 94720, United States; carter-fenk@berkeley.edu, Martin Head-Gordon – Kenneth S. Pitzer Center for Theoretical Chemistry, Department of Chemistry, University of California, Berkeley, California 94720, United States; Chemical Sciences Division, Lawrence Berkeley National Laboratory, Berkeley, California 94720, United States; mhg@cchem.berkeley.edu, Krupa Ramasesha – Combustion Research Facility, Sandia National Laboratories, Livermore, California 94550, United States; kramase@sandia.gov.

[||]J.T. and K.C.-F contributed equally to this work.

Kenneth S. Pitzer Center for Theoretical Chemistry, Department of Chemistry, University of California, Berkeley, California 94720, United States; Chemical Sciences Division, Lawrence Berkeley National Laboratory, Berkeley, California 94720, United States;

Krupa Ramasesha
Combustion Research Facility, Sandia National Laboratories, Livermore, California 94550, United States;

Abstract

In typical carbonyl-containing molecules, bond dissociation events follow initial excitation to $n\pi^*_{C=O}$ states. However, in acetyl iodide, the iodine atom gives rise to electronic states with mixed $n\pi^*_{C=O}$ and $n\sigma^*_{C-I}$ character, leading to complex excited-state dynamics, ultimately resulting in dissociation. Using ultrafast extreme ultraviolet (XUV) transient absorption spectroscopy and quantum chemical calculations, we present an investigation of the primary photodissociation dynamics of acetyl iodide via time-resolved spectroscopy of core-to-valence transitions of the I atom after 266 nm excitation. The probed I 4d-to-valence transitions show features that evolve on sub-100-fs time scales, reporting on excited-state wavepacket evolution during dissociation. These features subsequently evolve to yield spectral signatures corresponding to free iodine atoms in their spin–orbit ground and excited states with a branching ratio of 1.1:1 following dissociation of the C–I bond. Calculations of the valence excitation spectrum via equation-of-motion coupled cluster with single and double substitutions (EOM-CCSD) show that initial excited states are of spin-mixed character. From the initially pumped spin-mixed state, we use a combination of time-dependent density functional theory (TDDFT)-driven nonadiabatic *ab initio* molecular dynamics and EOM-CCSD calculations of the $N_{4,5}$ edge to reveal a sharp inflection point in the transient XUV signal that corresponds to rapid C–I homolysis. By examining the molecular orbitals involved in the core-level excitations at and around this inflection point, we are able to piece together a detailed picture of C–I bond photolysis in which $d \rightarrow \sigma^*$ transitions give way to $d \rightarrow p$ excitations as the bond dissociates. We also report theoretical predictions of short-lived, weak $4d \rightarrow 5d$ transitions in acetyl iodide, validated by weak bleaching in the experimental transient XUV spectra. This joint experimental–theoretical effort has thus unraveled the detailed electronic structure and dynamics of a strongly spin–orbit coupled system.

Graphical Abstract
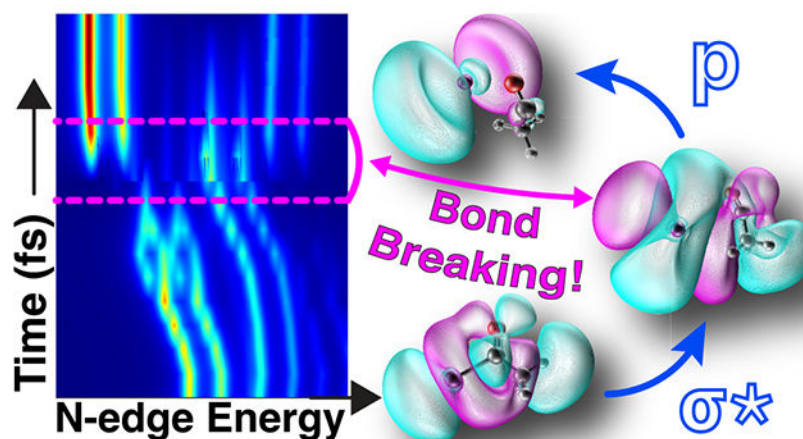
I. INTRODUCTION

Photodissociation of gas-phase organic molecules has been of keen interest to physical chemists for decades due to both its relevance to photochemical reactions in the atmosphere[1–5] and the opportunity it provides to understand electronic excited-state dynamics arising from the breakdown of the Born–Oppenheimer approximation.[6–9] A significant proportion of these studies have focused on the photodissociation dynamics of carbonyl-containing organic molecules[10–23] and alkyl halides,[24–27] which are both reported to play important roles in photochemical reactions in the atmosphere.[28–30] In carbonyl-containing molecules such as aliphatic aldehydes and ketones, it is well known that near-UV excitation of the $n \rightarrow \pi_{CO}^*$ transition leads to photodissociation via the Norrish type I process, where intersystem crossing (ISC) to the $^3n\pi^*$ state results in cleavage of the a-C–C bond. Furthermore, depending on the excitation wavelength, small aldehydes and ketones can also dissociate into molecular products via a roaming mechanism.[31–35] In alkyl halides, on the other hand, near-UV excitation causes an $n \rightarrow n\sigma_{C-X}^*$ transition (X = halogen) within what is known as the Aband consisting of close-lying, strongly dissociative states. Excitation to these dissociative states ultimately leads to the ultrafast dissociation of the C–X bond, yielding an alkyl radical and a halogen atom. The halogen is typically formed in both its ground and spin–orbit excited states due to bifurcation of the excited-state wavepacket at conical intersections along the dissociation coordinate.[36]

Acetyl halides ($CH_3C(O)X$, henceforth AcX), which contain both C=O and C–X chromophores, serve as a unique class of molecules in which competing photodissociation pathways arise due to the involvement of both $n\pi_{C=O}^*$ and $n\sigma_{C-X}^*$ states. The investigation of acetyl halide photodissociation has been the subject of several publications examining the energy content of the dissociation end-products.[37–41] Of the acetyl halides, AcCl is the most extensively studied system.[41–53] The UV absorption spectrum of AcCl shows a $n\pi^*$ absorption band centered at 240 nm;[54] the $n\sigma^*$ band in AcCl is expected to be in the deep-UV region around 170–200 nm and thus is well separated in energy from the $n\pi^*$ state.[55,56] Butler and co-workers showed that despite the similar bond energies of the a-C–C and a-C–Cl bonds in acetyl chloride, 248 nm excitation of this molecule to the $n\pi^*$ state first results

in the prompt dissociation of the C–Cl bond over a barrier formed from an avoided crossing with the $n\sigma^*_{C-Cl}$ state,[47] and the a-C–C bond is cleaved only via slower secondary dissociation of the acetyl radical. Thus, unlike the Norrish type I pathway in aliphatic aldehydes and ketones following ISC, the primary dissociation in AcCl is thought to occur on singlet states on ultrafast time scales. The time scale for the primary dissociation was estimated in photofragment translational spectroscopy and velocity map imaging experiments via the large observed anisotropy parameter, suggesting that the CH_3CO and Cl/Cl* fragments are formed on time scales faster than the ~70 ps rotational period of the parent molecule (based on rotational constants of AcCl from ref. 57). The isotropic angular distributions of the CH_3 and CO photofragments formed from secondary dissociation of the acetyl radical after excitation at 236 nm[43] suggested that secondary dissociation happens on time scales much longer than the rotational period. Ultrafast time-resolved studies of AcCl photodissociation by Suzuki et al. at 253 nm using multiphoton ionization and photofragment ion imaging found prompt fission into an acetyl radical and Cl within their instrument time resolution of 200 fs,[58] followed by secondary dissociation on a hundreds of picoseconds time scale, in agreement with previous estimates.[59]

Fewer studies exist on the UV photodissociation of AcBr than AcCl,[40,60–62] and neither ultrafast time-resolved studies nor theoretical and experimental characterization of electronic excited states has been performed on this system. Unlike in AcCl where a UV photon at 220–300 nm unambiguously causes an $n \rightarrow \pi^*$ transition, the character of the excited states in AcBr at these wavelengths is uncertain. In AcBr, 234 and 248 nm excitation has been shown to indeed result in primary C–Br dissociation followed by slow secondary dissociation of the acetyl radical, though it is unclear whether the C–Br dissociation occurs due to direct excitation to the $n\sigma^*_{C-Br}$ state[40] as in alkyl halides or whether UV excitation first populates the $n\pi^*$ state followed by dissociation on the $n\sigma^*_{C-Br}$ state, as in AcCl.[60] This ambiguity arises as two absorption bands, centered at 210 and 240 nm, may cause excitation to states of varying character. The absorption band centered at 210 nm that Lee et al.[40] report to be of $n\sigma^*_{C-Br}$ character may also have nonvanishing absorption past 230 nm, opening the possibility of direct excitation to this state. Therefore, for excitation in the wavelength range of 234 to 248 nm, it is difficult to determine *a priori* which states might be populated.

As indicated above, the energy separation between the $n\pi^*_{C=O}$ and $n\sigma^*_{C-X}$ states decreases as a function of halogen substitution going down the period. Based on this trend, it is likely that the overlap of the $n\pi^*$ and $n\sigma^*$ absorption features is even more pronounced in AcI, thus resulting in valence electronic states of mixed character and leading to complex excited-state dynamics. This hypothesis may be supported by the fact that AcI reportedly exhibits at least 10 times larger absorption coefficients in the near-UV compared to other acetyl halides,[39,63] perhaps due to the larger oscillator strength of the $n\sigma^*_{C-I}$ transition. However, to the authors' knowledge, there have been no experimental or theoretical investigations of the valence electronic structure and ultrafast excited-state dynamics governing the photodissociation of AcI to rigorously test this hypothesis. The lone study on the photodissociation of AcI was performed by Kroger et al.[39] using photofragment translational spectroscopy following 266 nm excitation. Results from this work suggest anomalously fast secondary dissociation of the acetyl radical after the rapid loss of I from AcI. Based on the measured anisotropy and

calculations of the rotational period of the parent molecule, this work estimated time scales of 100 fs for the primary C–I bond dissociation and 10 ps for the secondary C–C bond dissociation.[39]

In this article, we present a joint experimental and theoretical effort geared toward characterizing the valence excited states accessed by 266 nm excitation and the subsequent ultrafast excited-state dynamics leading to the primary C–I bond dissociation in gas-phase acetyl iodide. Our experimental method of choice for this study is extreme ultraviolet time-resolved absorption spectroscopy (XUV-TRAS) due to its well-proven ability to combine site specificity with sensitivity to valence electronic structure. We use the equation-of-motion coupled-cluster (EOM-CCSD) theory for a robust characterization of the valence excited states of AcI accessed by 266 nm excitation. Our calculations confirm that the nature of valence states accessed at 266 nm is indeed a combination of $n \rightarrow \sigma^*$ and $n \rightarrow \pi^*$ character with strong spin–orbit coupling. Following 266 nm excitation, experimental transient core-level spectra capture the evolution of the excited-state wavepacket, revealing that primary C–I bond homolysis into acetyl radical and ground/spin–orbit excited iodine atoms occurs on a sub-100-fs time scale. A combination of time-dependent density functional theory (TDDFT)-driven nonadiabatic *ab initio* molecular dynamics and high-level EOM-CCSD calculations of the iodine $N_{4,5}$ edge allows a side-by-side comparison of theoretical and experimental XUV-TRAS spectra that corroborates sub-100-fs dissociation and reveals surprising contributions from weak, short-lived $4d \rightarrow 5d$ transitions.

Furthermore, due to the paucity of high-level electronic structure calculations of acetyl halides in general, we present new EOM-CCSD calculations on AcBr and AcCl, which serve to further contextualize our results on AcI. In particular, we find that the $n\sigma^*/n\pi^*$ mixing becomes more pronounced as a function of halogen atom mass, resulting in an AcCl spectrum that exhibits only $n \rightarrow \pi^*$ transitions, while the AcBr spectrum features low-energy $n\pi^*$ states along with the possibility of direct 220 nm excitation into an $n\sigma^*$ state (in accordance with Lee et al.),[40] with AcI exhibiting strong mixing between $n\sigma^*$ and $n\pi^*$ states throughout the entire spectrum. Overall, we find that the 266 nm accessible valence excited states of AcI, and therefore the photolysis dynamics, are fundamentally different from those of AcCl and AcBr due to strong spin–orbit coupling and the significant presence of low-energy $n \rightarrow \sigma^*$ transitions. Our combined experimental and theoretical results offer the first characterization of the $N_{4,5}$-edge spectrum of AcI as the excited-state wavepacket evolves in time, allowing a full characterization of the dynamical core-level spectrum that reveals unique and unanticipated spectral features that may offer great utility in future studies of the C–I dissociation process in a variety of systems.

II.   METHODS

II.A.   Experimental Methods.

Pulses centered at 800 nm with a 35 fs full width at half-maximum (FWHM) pulse duration and 3 mJ pulse energy from a commercial Ti:sapphire amplified laser system pump our XUV-TRAS apparatus; schematics of the system are available in a previous report.[64] The output from this laser is split equally by a beamsplitter into a pump and a probe arm. To generate the extreme ultraviolet (XUV) probe, the transmission through the beamsplitter is

focused by a f = 75 cm lens into a semi-infinite gas cell (SIGC) that is filled with neon gas and held at a pressure of 50 Torr to produce XUV via high harmonic generation. Between the lens and the SIGC, a type-1 BBO crystal (100 μm thick, cut for second-harmonic generation) generates a weak second-harmonic field (10% conversion efficiency). A dual wave plate rotates the polarization of the 800 nm to match the polarization of the 400 nm, and two calcite plates (thickness of 750 μm) temporally and spatially overlap the 800 and 400 nm beams in the SIGC by compensating for the temporal walk-off between the two colors introduced by the dual waveplate and a 2-mm-thick CaF_2 entrance window of the SIGC. The two-color field enables the generation of even and odd harmonics to achieve the necessary spectral coverage for transient absorption measurements. The output from the SIGC is then filtered by a 200-nm-thick Al filter to transmit XUV between 15 and 72.7 eV and block 800 and 400 nm. A toroidal mirror focuses the generated XUV on the interaction region, where a sample cell is placed. The XUV transmitted through the sample passes through a second, 600-nm-thick Al filter and is collected and frequency-resolved by a flat-field concave grating (Hitachi) and detected on an X-ray CCD camera (Andor Newton 840), resulting in an energy resolution of 15 meV at 44 eV and 40 meV at 72 eV.

The pump arm uses the reflected portion of the 50:50 beam splitter. The reflected 800 nm beam is first sent onto a retroreflector mounted on a motorized linear stage to provide a computer-controlled delay between the pump and probe pulses, allowing us to change the delay t stepwise in increments of 2.2 fs over a range of 660 ps. After the beam passes through a type-1 BBO crystal for second-harmonic generation (200 μm thickness), a calcite plate (900 μm thickness), a dual wave plate, and a type-1 BBO crystal for third harmonic generation (100 μm thickness), we use wavelength-separating dielectric mirrors that are coated to reflect 266 nm (reflectance >95%) and transmit 400 and 800 nm (transmittance >90%). We found that reflection off five wavelength-separating mirrors is sufficient to fully suppress any 400 and 800 nm. An f = 1 m CaF_2 lens focuses the 266 nm spectra into the sample cell. Inside the vacuum chamber and halfway between the lens and the sample gas cell, a 45° dielectric mirror reflects the 266 nm and sends it into the sample cell noncollinearly at an angle of ~0.8° with respect to the XUV. A beam block is inserted into the 266 nm beam after the sample cell to further reduce any 266 nm scatter from entering the XUV spectrometer. Pulse energies (266 nm) of up to 40 μJ can be generated.

In the interaction region, the sample gas flow cell is 10 mm long and contains 600-μm-diameter holes for the XUV and 266 nm beams to pass though. The internal volume of the cell is 68 mm^3. Acetyl iodide (99% purity, Sigma-Aldrich) is flowed at room temperature with a static pressure of 5 Torr in the flow cell. Pump power studies (see Supporting Information Figure S7) for AcI reveal a one-photon dependence of signal intensity as a function of 266 nm pulse energy in the range of 1–12 μJ, with a clear saturation effect for pulse energies greater than 15 μJ per pulse; we used 10 μJ 266 nm pulse energy for all of the data reported herein. The spot size at the sample position of the two-color field driving HHG is 90 × 90 μm^2, and the spot size of the 266 nm at the sample position is 110 × 140 μm^2.

We characterized the temporal instrument response function (IRF), assuming a Gaussian distribution, to be 74 ± 3 fs FWHM (σ_{IRF} = 44 ± 2 fs) via the ponderomotive upshift of the atomic Xe resonance associated with the $^2D_{5/2} \rightarrow {}^2P_{3/2}$ core-excited Rydberg state

at 65.1 eV.[65,66] The ponderomotive shift of this transition to 65.3 eV is limited to the duration of UV and XUV and can therefore be used as a measurement of the IRF. The experimentally measured pump–probe cross correlation is given in Figure S8 in the SI. We use this measurement also to determine the location of the pump–probe temporal overlap (t_0).

For the polarization-dependent measurements reported in the Supporting Information, we switched the polarization of the 266 nm light between s- and p-polarization while keeping the XUV at p-polarization. At each time delay, we collected 920 spectra for the parallel polarization configuration and 450 spectra for the perpendicular polarization configuration. Each spectrum was collected with an exposure of 80 laser shots, and the delay points were collected in a randomized fashion, resulting in a noise level of $\sigma \approx 1.4$ mOD (mean in energy), measured as the standard error of the mean. The noise floor was suppressed during data analysis by applying adaptive iteratively reweighted principal component regression (airPCR),[67] which reduced the noise level to $\sigma \approx 0.8$ mOD (mean in energy).

For the UV/vis measurement of AcI, we employed a Lambda 1050+ UV/vis spectrophotometer from PerkinElmer. A few drops of AcI were placed in a cuvette in a dry nitrogen environment to avoid reaction with moisture. The cuvette was then quickly placed inside the spectrophotometer, and the absorption spectrum of gas-phase AcI at its ambient vapor pressure of approximately 32 Torr (at 298 K) was measured.[68] Various path length cuvettes were used to determine the optical density. Due to moisture slowly leaking into the cuvette and possible liquid-phase AcI contamination on the walls of the cuvette, no absolute cross section was determined.

II.B. Computational Methods.

The geometries of AcCl, AcBr, and AcI were optimized at the ωB97M-V/Def2-ma-TZVPP level of theory.[69–71] With these structures, we computed valence spectra using EOM-CCSD. We use the Def2-ma-TZVP basis set for C and O atoms and Def2-TZVP for H, and for the halogen atoms, we use the all-electron x2c-TZVPall-2c basis set optimized for scalar one- and two-component relativistic calculations[72] that we further augment with diffuse functions from the Def2-ma-TZVP basis set.[71,73]

Next, we use a combination of ORCA v5.0.3[74] and SHARC v2.1[75–77] to run nonadiabatic *ab initio* molecular dynamics (*ai*MD) using Tully's fewest switches surface-hopping (FSSH) approach to model the electronic populations.[78–80] The SHARC program allows us to include nonadiabatic and spin–orbit couplings between the five singlet and five triplet electronic states that we model throughout a 100 fs NVE simulation with 0.5 fs time steps. To model the nonadiabatic dynamics, we employ TDDFT with the ωB97X-D3 functional, which is one of the top performers for valence excited states.[81] We use a fine DefGrid3[82] quadrature to evaluate the exchange-correlation potential and account for scalar relativistic effects through the second-order Douglas–Kroll–Hess Hamiltonian,[83–85] along with a perturbative *ab initio* treatment of spin–orbit couplings via the Breit–Pauli Hamiltonian.[86] Prior to using TDDFT to model the dynamics of AcI, we ensured that the valence spectra using TDDFT are qualitatively similar to those obtained with EOM-CCSD, which was indeed the case as shown in Figure S1. Finally, the cc-pVDZ-DK basis set is used

for C, H, and O atoms with the aug-cc-pVTZ-DK basis on I for all TDDFT-based *ai*MD calculations.[87–89]

Interestingly, we found a large number of spurious high-intensity peaks in preliminary TDDFT calculations of the $N_{4,5}$-edge spectra (Figure S9), which may be due to a lack of orbital relaxation[90,91] but whose origins are unknown. Most concerning is the fact that many of these spurious transitions appear within the 40–50 eV energy range where we expect strong absorption from the free I atom, which could obfuscate the results. Therefore, all $N_{4,5}$-edge spectra are calculated using EOM-CCSD with spin-polarized orbitals in the all-electron x2c-SVPall-2c basis set that is again modified with diffuse functions, this time from the corresponding Def2-SVPD basis set.[73] Henceforth, we refer to the resultant basis set as x2c-SVPDall-2c. We decouple the core states from the valence excitations using the core–valence separation (CVS) scheme of Krylov and Coriani.[92] This CVS-EOM-CCSD scheme differs from the original Coriani and Koch approach[93] in that the core electrons are frozen when the ground-state coupled-cluster amplitudes are calculated. Furthermore, we decouple transitions out of each d orbital from one another, as this stabilizes convergence and reduces the number of roots required to compute the spectra. All $N_{4,5}$-edge spectra feature 30 roots/d orbital, and all EOM-CCSD and CVS-EOM-CCSD calculations are carried out using a development version of the Q-Chem v6.0.2 software package.[94]

We take both scalar and spin–orbit relativistic effects into consideration for all EOM-CCSD and CVS-EOM-CCSD calculations. In both cases, scalar relativistic effects are taken into account via a spin-free exact two-component (X2C) Hamiltonian.[95–101] For the valence EOM-CCSD calculations, we straightforwardly account for spin–orbit effects via the Breit-Pauli Hamiltonian,[102] but because we use spin-polarized orbitals for the CVS-EOM-CCSD calculations, the predicted core excited states are somewhat spin-contaminated. Consequently, we apply simpler atomic spin-orbit corrections to account for spin–orbit coupling in CVS-EOM-CCSD. As we are already decoupling the d orbitals of the I atom from the rest of the system when we calculate the CVS-EOM-CCSD amplitudes, we expect this to be a reasonable approximation. For the excited states, we average the d-orbital transition energies for each transition and apply an empirical $\omega + 3J_d$, $\omega - 2J_d$ doublet splitting where J_d is an empirical spin–orbit parameter that modulates the magnitude of the splitting. We set $J_d = 0.34$ eV in order to match the observed doublet splitting of 1.7 eV for the 4d orbitals of I.[103] The ground state of the I atom also exhibits substantial spin–orbit effects, with a doublet splitting of 0.9 eV between the $^2P_{1/2}$ and $^2P_{3/2}$ spin–orbit states. To resolve transitions out of both the true $^2P_{3/2}$ ground state and the $^2P_{1/2}$ state, we back-correct the ground-state reference energy, E_0, by accounting for the coupling between spin orbitals $|p_z\rangle \otimes |\uparrow\rangle$ and $|p_{x,y}\rangle \otimes |\downarrow\rangle$ (and vice versa). The corrected reference energy splits into $E_0 + 2J_p$ and $E_0 - J_p$ levels, therefore splitting the excitation energies into two spin–orbit channels,

$$\begin{aligned} \omega^{SO}(^2P_{3/2}) &= \omega^{NR} + J_p \\ \omega^{SO}(^2P_{1/2}) &= \omega^{NR} - 2J_p \end{aligned} \tag{1}$$

where ω^{NR} is the nonrelativistic excitation energy and $\omega^{SO}(X)$ is the spin–orbit-corrected excitation energies for each excitation channel, X. We set a value of $J_p = 0.3$ eV for

the ground state such that experimentally observed doublet splitting is achieved.[104,105] Finally, the intensities are scaled by the new excitation frequencies to satisfy the expected 2:3 ($^2D_{3/2}$:$^2D_{5/2}$) intensity ratio, and all forbidden $^2P_{1/2} \to {}^2D_{5/2}$ transitions are set to zero oscillator strength. This type of empirical treatment has been quite successful in the description of weak (J 0.5 eV) spin–orbit couplings; therefore, we expect it to perform similarly well here.[106,107]

III. RESULTS AND DISCUSSION

III.A. Valence Electronic Structure and UV/Vis Absorption Spectra of Acetyl Halides.

Due to limited characterization of the valence electronic structure of acetyl halides, particularly AcBr and AcI, we first present theoretical assignments of the UV/visible absorption spectra of acetyl halides with the goal of unraveling the valence excited-state transitions that contribute to the observed spectra. The top panel of Figure 1 juxtaposes EOM-CCSD results with the experimental absorption spectrum of AcCl. The experiment shows one broad absorption feature centered at 5.1 eV with an absorption cross section of approximately 0.1 MBarn. Our calculations predict one bright transition at 5.3 eV due to the $n \to \pi^*$ transition of singlet character, as expected from the existing literature. Repeating this exercise for AcBr in the middle panel of Figure 1, we see that the experimental spectrum consists of broad, overlapping features at 4.9 and 5.75 eV, resulting in a peak absorption cross section of approximately 0.3 MBarn. Our calculations reveal bands at 4.7, 5.0, and 5.8 eV. The 4.7 eV transition corresponds to direct excitation into the $^3n\pi^*$ state, while the one at 5.0 eV arises due to the $^1n\pi^*$ state. Interestingly, we find that the high-energy band at 5.8 eV emerges from direct population of the $^3n\sigma^*_{C-Br}$ state. Hence, our calculations are in agreement with the hypothesis of Lee et al.,[40] who proposed the possibility of direct UV excitation into a state of $n\sigma^*_{C-Br}$ character at 210 nm (5.9 eV). This finding has significant implications for AcBr photolysis and prompts further investigation of the electronic states involved in AcBr photodissociation dynamics.

Whereas published UV/vis absorption spectra exist for AcCl and AcBr over a range of wavelengths, the absorption cross section of AcI has been measured previously only by Etzler et al.[63] for a small set of wavelengths afforded by mercury emission lines. That work reports an increased absorption coefficient by a factor of approximately 10–20 in AcI compared to that in AcCl. Our experimental measurements extract an absorption cross section in excess of 2–6 MBarn; however, due to the reactivity of AcI with moisture and the lack of appropriate equipment for the rigorous measurement of cross sections, as mentioned in the Methods section, we refrain from reporting any definite numbers for its absorption cross section and limit our discussions to relative absorbance and peak locations. Our experimental UV/vis absorption spectrum of gas-phase AcI reveals absorption bands centered at 5.0 and 5.7 eV, along with a weak shoulder at 4.2 eV. The EOM-CCSD results in the bottom panel of Figure 1 show an offset of ~0.4 eV from the experimental results but remain in reasonable qualitative agreement with experiment, allowing us to make the most complete characterization of the spectrum as reported to date. The calculated spectrum (shifted by −0.425 eV) shows that the two overlapping features that make up the weak shoulder at 4.2 and 4.3 eV correspond to a combination of $n \to \pi^*$ and $n \to \sigma^*$ transitions

of mixed singlet and triplet character. The 5.0 eV feature is also composed of mixed-spin $n\pi^*$ and $n\sigma^*$ states, while the 5.6 eV feature can be attributed to a mixed-spin $n \rightarrow \pi^*$ transition. Interestingly, while the UV/visible absorption features in AcCl are dominated by $n \rightarrow \pi^*$ transitions, our results show that transitions of $n \rightarrow \sigma^*$ character become more important at lower energies as a function of halogen size. The $n\sigma^*$ states are responsible for just the highest-energy feature in AcBr, while in AcI they are found to be interspersed throughout the entirety of the spectrum. As spin–orbit coupling imposes strong mixing of the accessible states in AcI, we expect to populate largely spin-mixed states on excitation at 266 nm (4.7 eV).

III.B. XUV Absorption Spectrum of Ground-State Acetyl Iodide.

We now lay the groundwork for subsequent discussions of 266 nm excitation-induced changes in the XUV absorption spectrum of AcI near the $N_{4,5}$ edge by characterizing the ground-state core-level absorption spectrum. The experimental XUV absorption spectrum of AcI in Figure 2 exhibits sharp absorption features at 50.6, 52.2, 54.3, and 56 eV due to core-to-valence transitions from the iodine $4d$ orbitals to unoccupied valence orbitals. These four transitions together comprise two doublets that show the expected ~1.7 eV spin–orbit splitting of the $^2D_{5/2}$ and $^2D_{3/2}$ states with an I($4d$) core hole, suggesting that the atomic spin–orbit approximation outlined in the Computational Methods section is reasonable. The spin–orbit-corrected CVS-EOM-CCSD results align quite well with experiment, appearing only slightly shifted by ~0.6 eV relative to experimental features, which is well within the anticipated error margins of CVS-EOM-CCSD of roughly 1 to 2 eV[109] for core excitations. Our errors are likely somewhat smaller because of less-pronounced orbital relaxation effects in the $N_{4,5}$ edge relative to K-edge transitions.[110] We also note that the calculations overestimate the strength of the absorption of the higher-energy doublet at 54.3 and 56 eV. In any case, the straightforward comparison with experiment allows us to ascribe $d \rightarrow \sigma^*$ transitions to the features at 50.6 and 52.2 eV and transitions of mixed $d \rightarrow \sigma^*/\pi^*$ character to the higher-energy doublet features at 54.3 and 56 eV. As we will later discuss, the σ^* nature of these excited states is key to understanding the dynamics of C–I bond cleavage, so it is quite promising to see that $d \rightarrow \sigma^*$ transitions make up a significant contribution to both doublet features.

Though not clearly observed in the static XUV absorption spectrum of AcI, the CVS-EOM-CCSD calculations also predict several low-intensity peaks at 58.1, 59.6, 61.2, and 62.9 eV that correspond to $4d \rightarrow 5d$ transitions. While these $d \rightarrow d$ transitions are formally symmetry-forbidden, their weak intensity can be attributed to hybridization with orbitals on the acetyl group that acts to break the symmetry of the $5d$ orbitals. Some example $5d$ orbitals are shown in Figure S10. In principle, these $4d \rightarrow 5d$ transitions could be used to probe C–I bond breaking because as the I$\cdots C_2H_3O$ distance increases, they lose their hybridization with the C_2H_3O orbitals, thus becoming pure atomic $5d$ orbitals that strictly satisfy spatial symmetry selection rules. This should cause the $4d \rightarrow 5d$ transitions to be truly dark in the case of pure iodine and to gradually trend toward zero intensity as the C–I bond is broken. Indeed, in the case of a free I atom (as shown in Figure S14) there are no high-energy $4d \rightarrow 5d$ transitions in the spectrum. While no sharp absorption lines are observed above 56 eV in our experimental spectrum shown in Figure 2, we observe a broad, negative

differential absorbance on the order of <1 mOD surrounding the induced absorption features at 55.5 and 57.5 eV in Figure 3. Furthermore, Figure S3 clearly shows the persistent bleach signal that extends to 65 eV. It is potentially valuable to note that these high-energy features could provide a powerful spectroscopic handle for directly probing C–I dissociation in this and other related systems using attosecond XUV spectroscopy.

III.C. Transient XUV Absorption Spectra and Photodissociation Dynamics of Acetyl Iodide.

We performed XUV-TRAS in AcI in two orthogonal polarization configurations, and while these data show subtle differences in time-dependent behavior near t_0, we restrict our discussion to the data pertaining to parallel pump and probe polarization configurations where both the XUV and UV were p-polarized. (Perpendicular polarization data are reported in the Supporting Information.)

Figure 3a shows a two-dimensional false color map of the change in optical density after 266 nm excitation as a function of the time delay between pump and probe for XUV photon energies of 43 to 60 eV. The location of t_0, when pump and probe coincide in time, is defined by a time-zero measurement in xenon gas, as described in the Experimental Methods section. Measurements of the transient signal were performed in a time window from −300 to 1000 fs, with a 7 fs step size around t_0 to sufficiently sample the early dynamics. Positive delay values indicate the pump pulse preceding the probe pulse. After the first 250 fs, no changes in the differential absorbance are present, and as such, we show data only up to 300 fs in delay. (See Figure S4 for the false color map out to 1 ps.)

At long time delays ($t > 100$ fs), the differential absorption displayed in Figure 3 (and in Figure S3 as an outline) shows bleach features (defined as a negative absorption change) at 50.6, 52.2, 54.3, and 56 eV associated with the depletion of ground-state AcI and induced absorption features (defined as positive absorption changes) associated with atomic resonances of iodine previously assigned to transitions in ground-state I from $^2P_{3/2} \rightarrow$ $^2D_{5/2}$ at 46.1 eV, $^2P_{3/2} \rightarrow {}^2D_{3/2}$ at 47.8 eV, and $4d \rightarrow 6p/7p$ at 55.5 and 57.5 eV and spin–orbit excited I*($^2P_{1/2} \rightarrow {}^2D_{3/2}$) at 46.8 eV.[111] The atomic iodine features show a spectral width of ~300 meV FWHM, and the experimentally measured branching ratio of I*($^2P_{1/2}$ $\rightarrow {}^2D_{3/2}$):I($^2P_{3/2} \rightarrow {}^2D_{5/2}$) is 1:1.1, after taking into account the differences in the oscillator strengths between the core-level transitions of I and I*.[36,112] For comparison, in AcCl, the ratio Cl*:Cl is reported to be 3.3:1,[41] and in AcBr, the ratio Br*:Br is 1:2.[40] Dissociation of the C–I bond in methyl iodide has been reported to yield a I*:I ratio of 3:1,[26] whereas in i-C_3H_7I (nearly the same molecular mass as acetyl iodide), an I*:I ratio of 1:2 was observed.[36] In alkyl iodides, trends in this ratio as a function of alkyl substitution have been attributed to differences in wavepacket bifurcation at a conical intersection between two electronic states along the dissociation coordinate.[36] In AcI, however, cuts through the potential energy surfaces, as shown in Figure S11, reveal the involvement of multiple electronic states in the dissociation dynamics. This is corroborated by the time-dependent state populations extracted from our *ai*MD simulations (Figure S12), which show that many electronic states participate in the nonadiabatic dynamics leading up to C–I bond

dissociation. With so many states involved, a straightforward interpretation of this ratio is complicated.

At short time delays ($t < 100$ fs), additional features are visible near t_0. Figure 3b,c shows the most significant changes on a sub-100-fs time scale seen in the experiment. Aside from the bleach features associated with the loss of ground-state AcI and induced absorption features due to free I/I*, we observe a weak, short-lived feature at 47.1 eV (indicated by an arrow in panel (c)). We also observe a shift in the time-resolved differential absorbance at 55.3 eV, which undergoes a center-of-mass shift to 55.5 eV in less than 200 fs, as shown in Figure 3b.

In Figure 4, we present outlines and fits of selected features as a function of the pump–probe delay. At t_0, the bleach associated with AcI and induced absorption associated with free iodine rise promptly and reach an asymptotic plateau within the first 150 fs. We thus fit this steplike time evolution of these transient features to a Gaussian cumulative distribution function (CDF) convolved with our IRF ($\sigma_{IRF} = 44$ fs). The bleach features at 50.6 and 52.2 eV are measured with a temporal width (σ) of 41 ± 8 fs and no measurable offset with respect to t_0. The induced absorption features associated with free iodine at 46.1 and 46.8 eV both show identical temporal behavior, best described by a CDF with a σ of 47 ± 5 fs and an offset in time of 24 ± 7 fs with respect to t_0. The short-lived feature at 47.1 eV spectrally overlaps with the induced absorption at 46.8 eV, and hence we subtract a scaled CDF function that characterizes the step response of the neighboring induced absorption at 46.8 eV (as detailed in Figure S5 of the Supporting Information). After this subtraction, it is clear that the 47.1 eV feature is mostly confined around t_0. An exponential decay fit (convolved with the IRF) to the time profile of this feature yields an offset of 35 ± 15 fs from t_0 and a temporal width of $\sigma = 30 \pm 10$ fs. For the 55.5 eV feature, a fit to the shift in energy results in a CDF with a σ of 60 ± 37 fs and an offset in time of -8 ± 27 fs, while a fit to its amplitude using a CDF extracts a σ of 48 ± 20 fs and an offset in time of 60 ± 15 fs. The induced absorption at 57.5 eV does not show a shift in energy but rises with a σ of 89 ± 12 fs and an offset of 84 ± 9 fs.

To begin understanding the dynamics after 266 nm excitation, Figure S11 presents cuts through the potential energy surface for pure singlet and triplet states in AcI as a function of C–I displacement from its equilibrium bond length. This reveals that all spin-pure excited states are inherently dissociative, suggesting that we should expect prompt dissociation of the C–I bond on any optical transition that is accessible via the 266 nm pump. Indeed, our nonadiabatic and spin–orbit-inclusive *ai*MD simulations corroborate this notion. We begin the dynamics in the lowest-energy bright spin–orbit state (root 12, at 254 nm/4.9 eV) that is most likely to be excited by the 266 nm pump pulse, and we see immediate C–I bond dissociation. We track $\langle \hat{S}^2 \rangle$ of the excited state (Figure S13) as a simple metric for bond breaking, as we expect the formation of two doublet radicals homolytic bond cleavage) or $\langle \hat{S}^2 \rangle = 2$ corresponding to a triplet final state. This supposition is verified by examining the lowest-energy excited state in Figure S11, which is a triplet that corresponds to a spin-flip excitation ($p_I \rightarrow n_{Ac}$) out of the doubly occupied p orbital in a spin-restricted reference,

leading to separated I and CH_3CO radicals with an overall triplet multiplicity. $\langle \hat{s}^2 \rangle$ tracks well with the C–I distance and reaches a pure triplet state by just 50 fs after initial excitation, corroborating the notion of prompt C–I photolysis. Notably, this metric also correlates very well with the collapse of state populations in Figure S12, wherein many states are involved during the suspected bond-breaking timeline between 30 and 50 fs followed by a collapse into two triplet states that oscillate back and forth after 50 fs due to quasi-degeneracy.

The CVS-EOM-CCSD spectrum of the I atom (Figure S14) helps to contextualize the spectra of AcI at various points throughout the dynamics. Iodine ($^2P_{3/2}$) exhibits a low-energy doublet with peaks at 45.8 and 47.5 eV that are due to $d \rightarrow 5p(\beta)$ transitions into the vacant β spin orbital along with a high-energy doublet at 56 and 57.7 eV due to $d \rightarrow 5p(\alpha)$ transitions. Spin–orbit excited I($^2P_{1/2}$) leads to just two peaks at 46.6 and 56.8 eV rather than two doublets because the $^2P_{1/2} \rightarrow {}^2D_{5/2}$ transitions are forbidden. Importantly, iodine lacks any of the high-energy $4d \rightarrow 5d$ transitions that appear above 56 eV in AcI.

Turning our gaze toward the dynamical picture in Figure 5, we can see the rapid trend in the AcI $N_{4,5}$-edge spectrum toward that of pure iodine. By just 80 fs, the spectrum more strongly resembles free I and spin–orbit excited I* than that of t_0 acetyl iodide, again supporting sub-100-fs C–I dissociation.

To show the temporal evolution of the AcI $N_{4,5}$-edge spectrum toward I/I* and C_2H_3O, we computed CVS-EOM-CCSD spectra at 5 fs increments throughout the *ai*MD trajectory and constructed the heat map in Figure 5. From the outset at $t = 0$ fs until around 50 fs, there is a significant red shift of all peaks in AcI as the C–I bond distance increases, with the exception of one $4d \rightarrow 5d$ transition at 63 eV that features a slight blue shift. Interestingly, at times >50 fs the higher-energy doublet hits an inflection point and begins to sharply blue shift. Due to the finite experimental time resolution, this blue shift, manifested clearly in the feature at 55.3 eV, is all that is observed in the experiment (Figure 3b). Interestingly, even at 80 fs, the calculated $4d \rightarrow 6p$ transitions at 55.6 eV remain red-shifted from the $4d \rightarrow 6p$ transitions in free iodine by ~0.3 eV, implying residual (nonbonding) interactions between the acetyl radical and iodine fragments at times exceeding 80 fs. The residual interactions are more clearly seen in the $4d \rightarrow 6p$ bands than those associated with $4d \rightarrow 5p$ transitions, where the $4d \rightarrow 5p$ bands converge to the free-iodine result by about 60 fs. This can be justified by considering that core-excitation energies are strongly influenced by charge donor–acceptor interactions,[113] which are exponentially sensitive to orbital overlap. Because the 6p orbital is far more diffuse than the 5p orbital, it engages in donor/acceptor interaction with the acetyl fragment at longer I⋯CH_3CO distances and thus at longer times. We thus attribute the blue shift of the 55.3 eV feature seen in the experiment to shifting of the $4d \rightarrow 6p$ transition as the iodine continues to depart from the acetyl fragment.

More intriguing is that the C–I homolytic bond cleavage occurs right around 50 fs according to our $\langle \hat{s}^2 \rangle$ metric, which is precisely where we predict the inflection point in the high-energy doublet dynamics. The inflection point is punctuated by the disappearance of the $d_I \rightarrow \sigma^*_{AcI}$ transitions from the spectrum, giving way to $d_I \rightarrow p_I$ transitions that exhibit far less hybridization, thus taking on more of the character of the $d_I \rightarrow p_I$ excitations of free iodine

and shifting the excitation energies higher. We note that this inflection point occurs near the Coulson–Fischer point (yet another metric for bond breaking),[114] which we observe in coincidence with spin-symmetry breaking of the Hartree–Fock reference at times of 60 fs.

By shifting the focus to the low-energy doublet in Figure 5, we can see that the very last moments of C–I dissociation are captured by the experimental XUV-TRAS measurements. Namely, the short-lived 47.1 eV feature in Figure 3 can be understood as $d_I \rightarrow p_I/n_{Ac}$, where the primary transition is to a p orbital that is strongly mixed with the unoccupied n_{Ac} orbital on the acetyl fragment. This resolves by roughly 60 fs, where the C–I bond has been broken, leading to a primary transition of $d_I \rightarrow p_I$ character with very little orbital mixing. Therefore, we suspect that the 47.1 eV feature in the experiment is the footprint of a small fraction of AcI molecules on the cusp of full dissociation and that this signal rapidly merges with the brighter feature at 46.8 eV. Furthermore, the observed offset of 25 fs in the appearance of the experimental induced absorption corresponding to free iodine at 46.1 and 46.8 eV with respect to the instantaneous appearance of the bleach of AcI is due to a slightly delayed formation of free iodine following electronic excitation of AcI. This is consistent with our theory, which predicts that the growth of free iodine is delayed by 20 fs with respect to the loss of ground-state acetyl iodide signal.

We also note that the $4d \rightarrow 5d$ transitions predicted by CVS-EOM-CCSD that correspond to the doublets at energies >56 eV in AcI appear as weak features at early times but rapidly subside until they are no longer visible by roughly 40 fs. As we had predicted earlier, this is an indicator that the iodine $5d$ orbitals are no longer hybridizing with those of the acetyl fragment, taking on pure d-orbital symmetry. In the experiment, we detect a broad, unstructured bleach between 60 and 65 eV that appears promptly and can be associated with the loss of these transitions.

IV.   CONCLUSIONS

Herein, we present the first study of the ultrafast excited-state dynamics of acetyl iodide following 266 nm excitation. Our calculations using equation-of-motion coupled-cluster theory with single and double substitutions (EOM-CCSD) reveal that the valence excited states accessed by a 266 nm photon are spin-mixed and spin-pure singlets with $n\pi^*$ and $n\sigma^*$ character, which are dissociative along the C–I bond. Experimental time-resolved I $4d$-to-valence absorption spectra unveil spectral features that evolve on <100 fs time scales, which, through a combination of *ab initio* molecular dynamics (*ai*MD) simulations and EOM-CCSD, we ascribe to C–I bond dissociation dynamics. Specifically, EOM-CCSD calculations of the N-edge spectra along the *ai*MD trajectory show that spectral features of electronically excited AcI prior to dissociation correspond to $d_I \rightarrow \sigma_{AcI}^*$ transitions at early times that pass through a $d_I \rightarrow p_I/n_{Ac}$ intermediate on the verge of C–I bond breaking, finally giving way to $d_I \rightarrow p_I$ transitions of free I upon C–I dissociation. Additionally, calculations reveal the presence of $4d \rightarrow 5d$ transitions that are weakly allowed due to hybridization with the acetyl moiety in intact AcI, which proceed to disappear when the C–I bond breaks and these transitions become strictly forbidden. These predicted transitions turn out to be experimentally detectable as a broad unstructured bleach feature in the transient spectrum.

Whereas our calculations show that UV excitation of AcCl populates states of solely $n\pi^*$ character, valence-excited states in this energy range in AcI and AcBr also include participation of states of $n\sigma^*$ character. In AcBr, valence states at 4.7 and 5.0 eV have $n\pi^*$ character, while the state at 5.8 eV has $^3n\sigma^*_{C-Br}$ character. For AcI, we find that photodynamics are driven by the superposition of $n\pi^*$ and $n\sigma^*$ states with strongly mixed singlet and triplet character. This interplay of spin-pure singlet and spin-mixed states of different spatial symmetry is also in stark contrast to alkyl halides, where excited states have been described as having singlet or triplet $n\sigma^*$ character. The sub-100-fs lifetimes of the low-energy doublet in the 46–48 eV region observed here show parallels to the dynamics reported for alkyl iodide dissociation.[26,36] In addition, our study reveals and interprets sub-100-fs dynamics in the high-energy doublet near 55 eV, which, to the best of our knowledge, has not been done in ultrafast XUV studies of alkyl iodides.

Our joint experiment–theory investigation has provided spectroscopic signatures of the excited-state dynamics during the primary C–I bond dissociation in acetyl iodide. In particular, we identify avenues for future exploration on attosecond time scales for probing the coupled electronic and nuclear dynamics in real time by closely monitoring the spectral region associated with $4d \rightarrow 5d$ transitions. This article was restricted to the investigation of the primary dissociation of AcI; a follow-up time-resolved study of the secondary dissociation of the acetyl radical probed with soft X-ray spectroscopy of the carbon K-edge is forthcoming.

Supplementary Material

Refer to Web version on PubMed Central for supplementary material.

ACKNOWLEDGMENTS

REFERENCES

(1). Hasson AS; Tyndall GS; Orlando JJ A product yield study of the reaction of ho2 radicals with ethyl peroxy (C2H5O2), acetyl peroxy (CH3C(O)O2), and acetonyl peroxy (CH3C(O)CH2O2) radicals. J. Phys. Chem. A 2004, 108, 5979–5989.

(2). Vaida V; Solomon S; Richard EC; Rühl E; Jefferson A Photoisomerization of ocio: a possible mechanism for polar ozone depletion. Nature 1989, 342, 405–408.

(3). Lary DJ; Shallcross DE Central role of carbonyl compounds in atmospheric chemistry. J. Geophys. Res.: Atmos 2000, 105, 19771–19778.

(4). Kesselmeier J; Bode K; Gerlach C; Jork E-M Exchange of atmospheric formic and acetic acids with trees and crop plants under controlled chamber and purified air conditions. Atmos. Environ 1998, 32, 1765–1775.

(5). Grosjean D Formic acid and acetic acid: Emissions, atmospheric formation and dry deposition at two southern california locations. Atmos. Environ., Part A 1992, 26, 3279–3286.

(6). Curchod BFE; Martínez TJ Ab initio nonadiabatic quantum molecular dynamics. Chem. Rev 2018, 118, 3305–3336. [PubMed: 29465231]

(7). Butler LJ Chemical reaction dynamics beyond the bornoppenheimer approximation. Annu. Rev. Phys. Chem 1998, 49, 125–171. [PubMed: 15012427]

(8). Ischenko AA; Weber PM; Miller RJD Capturing chemistry in action with electrons: Realization of atomically resolved reaction dynamics. Chem. Rev 2017, 117, 11066–11124. [PubMed: 28590727]

(9). Adachi S; Schatteburg T; Humeniuk A; Mitri R; Suzuki T Probing ultrafast dynamics during and after passing through conical intersections. Phys. Chem. Chem. Phys 2019, 21, 13902–13905. [PubMed: 30259014]

(10). Diau EW-G; Kötting C; Zewail AH Femtochemistry of norrish type-i reactions: I. experimental and theoretical studies of acetone and related ketones on the S1 surface. ChemPhysChem 2001, 2, 273–293. [PubMed: 23696502]

(11). Houston PL; Kable SH Photodissociation of acetaldehyde as a second example of the roaming mechanism. Proc. Natl. Acad. Sci. U.S.A 2006, 103, 16079–16082. [PubMed: 17047035]

(12). Li H; Li Q; Mao W; Zhu Q; Kong F The ultraviolet photolysis of acetyl and propionyl radicals studied by infrared emission spectroscopy. J. Chem. Phys 1997, 106, 5943–5946.

(13). Mordaunt DH; Osborn DL; Neumark DM Nonstatistical unimolecular dissociation over a barrier. J. Chem. Phys 1998, 108, 2448–2457.

(14). Andreae MO; Talbot RW; Andreae TW; Harriss RC Formic and acetic acid over the central amazon region, brazil: 1. dry season. J. Geophys. Res.: Atmos 1988, 93, 1616–1624.

(15). Keene WC; Galloway JN; Holden JD Jr. Measurement of weak organic acidity in precipitation from remote areas of the world. J. Geophys. Res.: Oceans 1983, 88, 5122–5130.

(16). Kwon HT; Shin SK; Kim SK; Kim HL; Park CR Photodissociation dynamics of acetic acid and trifluoroacetic acid at 193 nm. J. Phys. Chem. A 2001, 105, 6775–6779.

(17). Singleton DL; Paraskevopoulos G; Irwin RS Rates and mechanism of the reactions of hydroxyl radicals with acetic, deuterated acetic, and propionic acids in the gas phase. J. Am. Chem. Soc 1989, 111, 5248–5251.

(18). Hunnicutt SS; Waits LD; Guest JA Energetic constraints in the 218 nm photolysis of acetic acid. J. Phys. Chem 1989, 93, 5188–5195.

(19). Hunnicutt SS; Waits LD; Guest JA $^1(n\pi*)$-photochemistry of acetic acid at 200 nm: further evidence for an exit channel barrier and reaction selectivity. J. Phys. Chem 1991, 95, 562–570.

(20). Yoon M-C; Choi YS; Kim SK Fluorescence excitation spectroscopic study of the jet-cooled acetyl cyanide. J. Phys. Chem 1999, 110, 7185–7191.

(21). Furlan A; Scheld HA; Huber JR The two competitive photodissociation channels in cyano carbonyls (NCC(O)X, X = CH3, CH(CH3)2, C(CH3)3, OCH3) at 193 nm. a study by photofragment translational energy spectroscopy. J. Phys. Chem. A 2000, 104, 1920–1929.

(22). Fang W-H; Liu R-Z; Zheng X; Phillips DL Photodissociation of acetic acid in the gas phase: An ab initio study. J. Org. Chem 2002, 67, 8407–8415. [PubMed: 12444618]

(23). Uenishi R; Horio T; Suzuki T Time-resolved photoelectron imaging of acetone with 9.3 ev photoexcitation. J. Phys. Chem. A 2019, 123, 6848–6853. [PubMed: 31314525]

(24). Riley SJ; Wilson KR Excited fragments from excited molecules: energy partitioning in the photodissociation of alkyl iodides. Faraday Discuss. Chem. Soc 1972, 53, 132–146.

(25). Wang G-J; Zhu R-S; Zhang H; Han K-L; He G-Z; Lou N-Q Photodissociation of chlorobenzene at 266 nm. Chem. Phys. Lett 1998, 288, 429–432.

(26). Attar AR; Bhattacherjee A; Leone SR Direct observation of the transition-state region in the photodissociation of CH3I by femtosecond extreme ultraviolet transient absorption spectroscopy. J. Phys. Chem. Lett 2015, 6, 5072–5077. [PubMed: 26636176]

(27). Heald LF; Loftus CL; Gosman RS; Sayres SG Ion-pair formation in n-butyl bromide through 5p ryberg state predissociation. J. Phys. Chem. A 2022, 126, 9651–9657. [PubMed: 36528811]

(28). Lee J; Chen C-J; Bozzelli JW Thermochemical and kinetic analysis of the acetyl radical (CH3CO) + O2 reaction system. J. Phys. Chem. A 2002, 106, 7155–7170.

(29). Carlier P; Hannachi H; Mouvier G The chemistry of carbonyl compounds in the atmosphereâ€' a review. Atmos. Environ. (1967–1989) 1986, 20, 2079–2099.

(30). Herndon SC; Gierczak T; Talukdar RK; Ravishankara AR Kinetics of the reactions of OH with several alkyl halides. Phys. Chem. Chem. Phys 2001, 3, 4529–4535.

(31). Jacob LSD; Lee KLK; Schmidt TW; Nauta K; Kable SH The dynamics of co production from the photolysis of acetone across the whole S1 ← S0 absorption spectrum: Roaming and triple fragmentation pathways. J. Chem. Phys 2022, 156, 094303. [PubMed: 35259892]

(32). Toulson BW; Fishman DA; Murray C Photodissociation dynamics of acetone studied by time-resolved ion imaging and photofragment excitation spectroscopy. Phys. Chem. Chem. Phys 2018, 20, 2457–2469. [PubMed: 29313039]

(33). Owrutsky JC; Baronavski AP Ultrafast photodissociation dynamics of the s1 and s2 states of acetone. J. Chem. Phys 1999, 110, 11206–11213.

(34). Lee KLK; Nauta K; Kable SH Photodissociation of acetone from 266 to 312 nm: Dynamics of CH3 + CH3CO channels on the S0 and T1 states. J. Chem. Phys 2017, 146, 044304. [PubMed: 28147527]

(35). Goncharov V; Herath N; Suits AG Roaming dynamics in acetone dissociation. J. Phys. Chem. A 2008, 112, 9423–9428. [PubMed: 18588266]

(36). Chang KF; Wang H; Poullain SM; González-Vázquez J; Bañares L; Prendergast D; Neumark DM; Leone SR Conical intersection and coherent vibrational dynamics in alkyl iodides captured by attosecond transient absorption spectroscopy. J. Chem. Phys 2022, 156, 114304. [PubMed: 35317567]

(37). North S; Blank DA; Lee YT Determination of the barrier height to CH3CO dissociation. Chem. Phys. Lett 1994, 224, 38–42.

(38). Song X A theoretical study on the photodissociation mechanism of acetyl fluoride (CH3C(O)F) involving S0, S1, and T1 states. Chem. Phys 2017, 491, 95–101.

(39). Kroger PM; Riley SJ Dynamics of three-body half collisions. i. secondary product decomposition in the photodissociation of acetyl iodide. J. Phys. Chem 1977, 67, 4483–4490.

(40). Lee KW; Jee Y-J; Jung K-H Photodissociation dynamics of acetyl bromide at 234 nm. J. Chem. Phys 2002, 116, 4490–4496.

(41). Tang X; Ratliff BJ; FitzPatrick BL; Butler LJ Determination of the barrier height for acetyl radical dissociation from acetyl chloride photodissociation at 235 nm using velocity map imaging. J. Phys. Chem. B 2008, 112, 16050–16058. [PubMed: 19367922]

(42). Womack CC; Fang W-H; Straus DB; Butler LJ Assessing an impulsive model for rotational energy partitioning to acetyl radicals from the photodissociation of acetyl chloride at 235 nm. J. Phys. Chem. A 2010, 114, 13005–13010. [PubMed: 21117659]

(43). Deshmukh S; Hess WP Photodissociation of acetyl chloride: Cl and CH3 quantum yields and energy distributions. J. Phys. Chem 1994, 100, 6429–6433.

(44). Chen S-L; Fang W-H Insights into mechanistic photodissociation of acetyl chloride by ab initio calculations and molecular dynamics simulations. J. Phys. Chem. A 2007, 111, 9355–9361. [PubMed: 17683127]

(45). Liu Y-T; Tsai M-T; Liu C-Y; Tsai P-Y; Lin K-C; Shih YH; Chang AHH Photodissociation of gaseous acetyl chloride at 248 nm by time-resolved fourier-transform infrared spectroscopy: The HCl, CO, and CH2 product channels. J. Phys. Chem. A 2010, 114, 7275–7283. [PubMed: 20568795]

(46). Deshmukh S; Myers JD; Xantheas SS; Hess WP Investigation of acetyl chloride photodissociation by photofragment imaging. J. Phys. Chem 1994, 98, 12535–12544.

(47). Person MD; Kash PW; Butler LJ Nonadiabaticity and the competition between alpha and beta bond fission upon $^1[n, \pi(C = O)]$ excitation in acetyl- and bromoacetyl chloride. J. Phys. Chem 1992, 97, 355–373.

(48). Person MD; Kash PW; Butler LJ A new class of norrish type i processes: .alpha.-bond cleavage upon 1(nπ*(C = O)) excitation in the acid halides. J. Phys. Chem 1992, 96, 2021–2023.

(49). Sumathi R; Chandra AK Photodecomposition of acetyl chloride on the excited singlet state surface. J. Phys. Chem 1993, 99, 6531–6536.

(50). Arunan E The C-C bond is stronger than the C-Cl bond in CH3COCl. J. Phys. Chem. A 1997, 101, 4838–4839.

(51). Kogure N; Ono T; Suzuki E; Watari F Photolysis of matrix-isolated acetyl chloride and infrared spectrum of the 1:1 molecular complex of hydrogen chloride with ketene in solid argon. J. Mol. Struct 1993, 296, 1–4.

(52). Rowland B; Hess WP The ultraviolet photochemistry of condensed-phase acetyl chloride. Chem. Phys. Lett 1996, 263, 574–580.

(53). Rowland B; Hess WP Uv photochemistry of thin film and matrix-isolated acetyl chloride by polarized ftir. J. Phys. Chem. A 1997, 101, 8049–8056.

(54). Thompson KC; Crittenden DL; Kable SH; Jordan MJT A classical trajectory study of the photodissociation of t1 acetaldehyde: The transition from impulsive to statistical dynamics. J. Phys. Chem 2006, 124, 044302.

(55). Eden S; Limao-Vieira P; Hoffmann SV; Mason NJ Vuv spectroscopy of CH3Cl and CH3I. Chem. Phys 2007, 331, 232–244.

(56). Browning PW; Kitchen DC; Arendt MF; Butler LJ Investigating the c-cl antibonding character in the $\pi\pi$* excited state of vinyl, allyl, and propargyl chloride: Emission spectra and ab initio calculations. J. Phys. Chem 1996, 100, 7765–7771.

(57). Durig JR; Davis JF; Guirgis GA Raman and far infrared spectra, structural parameters, and ab initio calculations on acetyl chloride. J. Raman Spectrosc 1994, 25, 189–198.

(58). Shibata T; Suzuki T Photofragment ion imaging with femtosecond laser pulses. Chem. Phys. Lett 1996, 262, 115–119.

(59). Shibata T; Li H; Katayanagi H; Suzuki T Dissociation of metastable CH3CO radical observed by subpicosecond time-clocked photofragment imaging. J. Phys. Chem. A 1998, 102, 3643–3647.

(60). Lane IC; Meehan R; Powis I Interpretation of the photofragment anisotropy observed upon $n \rightarrow \pi_{CO}$ excitation of acetyl halides. J. Phys. Chem 1995, 99, 12371–12374.

(61). Su Y; Dibble T; Francisco J; Li Z Dissociation of acetyl bromide: an experimental and theoretical study. Chem. Phys 1995, 196, 59–67.

(62). Khamaganov V; Karunanandan R; Rodriguez A; Crowley JN Photolysis of CH3C(O)CH3 (248 nm, 266 nm), CH3C(O)C2H5 (248 nm) and CH3C(O)Br (248 nm): pressure dependent quantum yields of CH3 formation. Phys. Chem. Chem. Phys 2007, 9, 4098–4113. [PubMed: 17687461]

(63). Etzler D; Rollefson G The absorption coefficients of the acetyl halides. J. Phys. Chem 1938, 6, 653–653.

(64). Ramasesha K; Tross J; Schrader P; Sheps L; Au K TableTop High Photon Energy Sources for Chemical Dynamics Investigations; Technical Report; Sandia National Laboratory (SNL-NM): Albuquerque, NM, 2021.

(65). Lin M-F; Pfeiffer AN; Neumark DM; Leone SR; Gessner O Strong-field induced XUV transmission and multiplet splitting in 4d-16p core-excited xe studied by femtosecond XUV transient absorption spectroscopy. J. Chem. Phys 2012, 137, 244305. [PubMed: 23277934]

(66). Attar AR Photochemical reaction Dynamics Studied by Femtosecond Soft X-ray Transient Absorption Spectroscopy, Ph.D. Dissertation, University of California, Berkeley, CA, 2016.

(67). Faccialà D; Toulson BW; Gessner O Removal of correlated background in a high-order harmonic transient absorption spectra with principal component regression. Opt. Express 2021, 29, 35135–35148. [PubMed: 34808953]

(68). Devore JA; O'Neal HE Heats of formation of the acetyl halides and of the acetyl radical. J. Phys. Chem 1969, 73, 2644–2648.

(69). Mardirossian N; Head-Gordon M ωB97M-V: A combinatorially optimized, range-separated hybrid, meta-GGA density functional with VV10 nonlocal correlation. J. Chem. Phys 2016, 144, 214110. [PubMed: 27276948]

(70). Weigend F; Ahlrichs R Balanced basis sets of split valence, triple zeta valence and quadruple zeta valence quality for H to Rn: Design and assessment of accuracy. Phys. Chem. Chem. Phys 2005, 7, 3297–3305. [PubMed: 16240044]

(71). Zheng J; Xu X; Truhlar DG Minimally augmented Karlsruhe basis sets. Theor. Chem. Acc 2011, 128, 295–305.

(72). Pollak P; Weigend F Segmented contracted error-consistent basis sets of double- and triple-ζ valence quality for one- and two-component relativistic all-electron calculations. J. Chem. Theory Comput 2017, 13, 3696–3705. [PubMed: 28679044]

(73). Rappoport D; Furche F Property-optimized Gaussian basis sets for molecular response calculations. J. Chem. Phys 2010, 133, 134105. [PubMed: 20942521]

(74). Neese F; Wennmohs F; Becker U; Riplinger C The ORCA quantum chemistry program package. J. Chem. Phys 2020, 152, 224108. [PubMed: 32534543]

(75). Mai S; Richter M; Heindl M; Menger MFSJ; Atkins A; Ruckenbauer M; Plasser F; Ibele L; Kropf S; Oppel M; Marquetand P; González L SHARC2.1: Surface Hopping Including Arbitrary Couplings - Program Package for Non-Adiabatic Dynamics; sharc-md.org: SHARC, 2019.

(76). Richter M; Marquetand P; González-Vázquez J; Sola I; González L SHARC: *Ab initio* molecular dynamics with surface hopping in the adiabatic representation including arbitrary couplings. J. Chem. Theory Comput 2011, 7, 1253–1258; 2012, 8, 374. [PubMed: 26610121]

(77). Mai S; Marquetand P; González L Nonadiabatic dynamics: The SHARC approach. WIREs Comput. Mol. Sci 2018, 8, No. e1370. 1–23

(78). Tully JC; Preston RK Trajectory surface hopping approach to nonadiabatic molecular collisions: The reaction of H$^+$ with D$_2$. J. Chem. Phys 1971, 55, 562–572.

(79). Tully JC Molecular dynamics with electronic transitions. J. Chem. Phys 1990, 93, 1061–1071.

(80). Tully JC Perspective: Nonadiabatic dynamics theory. J. Chem. Phys 2012, 137, 22A301.

(81). Liang J; Feng X; ad M; Head-Gordon DH Revisiting the performance of time-dependent density functional theory for electronic excitations: Assessment of 43 popular and recently developed functionals from rungs one to four. J. Chem. Theory Comput 2022, 18, 3460–3473. [PubMed: 35533317]

(82). Helmich-Paris B; de Souza B; Neese F; Izsák R An improved chain of spheres for exchange algorithm. J. Chem. Phys 2021, 155, 104109. [PubMed: 34525816]

(83). Douglas M; Kroll NM Quantum electrodynamical corrections to the fine structure of helium. Ann. Phys 1974, 82, 89–155.

(84). Hess BA Applicability of the no-pair equation with free-particle projection operators to atomic and molecular structure calculations. Phys. Rev. A 1985, 32, 756–763.

(85). Hess BA Relativistic electronic-structure calculations employing a two-component no-pair formalism with external-field projection operators. Phys. Rev. A 1986, 33, 3742–3748.

(86). de Souza B; Farias G; Neese F; Izsák R Predicting phosphorescence rates of light organic molecules using time-dependent density functional theory and the path integral approach to dynamics. J. Chem. Theory Comput 2019, 15, 1896–1904. [PubMed: 30721046]

(87). Dunning TH Jr. Gaussian basis sets for use in correlated molecular calculations. I. The atoms boron through neon and hydrogen. J. Chem. Phys 1989, 90, 1007–1023.

(88). Kendall RA; Dunning TH Jr.; Harrison RJ Electron affinities of the first-row atoms revisited. Systematic basis sets and wave functions. J. Chem. Phys 1992, 96, 6796–6806.

(89). de Jong WA; Harrison RJ; Dixon DA Parallel Douglas-Kroll energy and gradients in NWChem: Estimating scalar relativistic effects using Douglas-Kroll contracted basis sets. J. Chem. Phys 2001, 114, 48–53.

(90). Carter-Fenk K; Cunha LA; Arias-Martinez JE; Head-Gordon M Electron-affinity time-dependent density functional theory: Formalism and applications to core-excited states. J. Phys. Chem. Lett 2022, 13, 9664–9672. [PubMed: 36215404]

(91). Carter-Fenk K; Head-Gordon M On the choice of reference orbitals for linear-response calculations of solution-phase K-edge X-ray absorption spectra. Phys. Chem. Chem. Phys 2022, 24, 26170–26179. [PubMed: 36278791]

(92). Vidal ML; Feng X; Epifanovsky E; Krylov AI; Coriani S New and efficient equation-of-motion coupled-cluster framework for core-excited and core-ionized states. J. Chem. Theory Comput 2019, 15, 3117–3133. [PubMed: 30964297]

(93). Coriani S; Koch H Communication: X-ray absorption spectra and core-ionization potentials within a core-valence separated coupled cluster framework. J. Chem. Phys 2015, 143, 181103. [PubMed: 26567637]

(94). Epifanovsky E; Gilbert ATB; Feng X; Lee J; Mao Y; Mardirossian N; Pokhilko P; White AF; Coons MP; Dempwolff AL; et al. Software for the frontiers of quantum chemistry: An overview of developments in the Q-Chem 5 package. J. Chem. Phys 2021, 155, 084801. [PubMed: 34470363]

(95). Dyall KG Interfacing relativistic and nonrelativistic methods. I. Normalized elimination of the small component in the modified Dirac equation. J. Chem. Phys 1997, 106, 9618–9626.

(96). Kutzelnigg W; Liu W Quasirelativistic theory equivalent to fully relativistic theory. J. Chem. Phys 2005, 123, 241102. [PubMed: 16396527]

(97). Iliaš M; Saue T An infinite-order two-component relativistic Hamiltonian by a simple one-step transformation. J. Chem. Phys 2007, 126, 064102. [PubMed: 17313208]

(98). Liu W; Peng D Exact two-component Hamiltonians revisited. J. Chem. Phys 2009, 131, 031104. [PubMed: 19624172]

(99). Saue T Relativistic Hamiltonians for Chemistry: A Primer. ChemPhysChem 2011, 12, 3077–3094. [PubMed: 22076930]

(100). Li Z; Xiao Y; Liu W On the spin separation of algebraic two-component relativistic Hamiltonians. J. Chem. Phys 2012, 137, 154114. [PubMed: 23083155]

(101). Cheng L; Gauss J Analytic energy gradients for the spin-free exact two-component theory using an exact block diagonalization for the one-electron Dirac Hamiltonian. J. Chem. Phys 2011, 135, 084114. [PubMed: 21895166]

(102). Vidal ML; Pokhilko P; Krylov AI; Coriani S Equation-ofmotion coupled-cluster theory to model L-edge X-ray absorption and photoelectron spectra. J. Phys. Chem. Lett 2020, 11, 8314–8321. [PubMed: 32897075]

(103). Nahon L; Duffy L; Morin P; Combet-Farnoux F; Tremblay J; Larzilliere M Relaxation of the 4d → 5p resonance in atomic iodine. Phys. Rev. A 1990, 41, 4879–4888. [PubMed: 9903711]

(104). Moore CE Atomic Energy Levels: As Derived from the Analyses of Optical Spectra; Circular National Bureau of Standards 467: Washington D. C., 1949; Vol. I.

(105). Huber KP; Herzberg G Molecular Spectra and Molecular Structure. IV. Constants of Diatomic Molecules; Van Nostrand Reinhold Co.: Princeton, NJ, 1979.

(106). Hait D; Head-Gordon M Highly accurate prediction of core spectra of molecules at density functional theory cost: Attaining sub-electronvolt error from a restricted open-shell Kohn–Sham approach. J. Phys. Chem. Lett 2020, 11, 775–786. [PubMed: 31917579]

(107). Cunha LA; Hait D; Kang R; Mao Y; Head-Gordon M Relativistic orbital-optimized density functional theory for accurate core-level spectroscopy. J. Phys. Chem. Lett 2022, 13, 3438–3449. [PubMed: 35412838]

(108). Keller-Rudek H; Moortgat GK; Sander R; Sörensen R The mpi-mainz uv/vis spectral atlas of gaseous molecules of atmospheric interest. Earth System Science Data 2013, 5, 365–373.

(109). Ranga S; Dutta AK A core–valence separated similarity transformed EOM-CCSD method for core-excitation spectra. J. Chem. Theory Comput 2021, 17, 7428–7446. [PubMed: 34814683]

(110). Jana D; Bandyopadhyay B; Mukherjee D Development and applications of a relaxation-inducing cluster expansion theory for treating strong relaxation and differential correlation effects. Theor. Chem. Acc 1999, 102, 317–327.

(111). Nahon L; Morin P Experimental study of rydberg states excited from the d shell of atomic bromine and iodine. Phys. Rev. A 1992, 45, 2887–2893. [PubMed: 9907320]

(112). Drescher L; Galbraith MCE; Reitsma G; Dura J; Zhavoronkov N; Patchkovskii S; Vrakking MJJ; Mikosch J Communication: Xuv transient absorption spectroscopy of iodo-methane and iodobenzene photodissociation. J. Chem. Phys 2016, 145, 011101. [PubMed: 27394091]

(113). Cremer T; Kolbeck C; Lovelock KRJ; Paape N; Wölfel R; Schulz PS; Wasserscheid P; Weber H; Thar J; Kirchner B; Maier F; Steinrück H-P Towards a molecular understanding of cation–anion interactions—probing the electronic structure of imidazolium ionic liquids by NMR spectroscopy, X-ray photoelectron spectroscopy and theoretical calculations. Chem.Eur. J 2010, 16, 9018–9033. [PubMed: 20658502]

(114). Coulson CA; Fischer I Notes on the molecular orbital treatment of the hydrogen molecule. Philos. Mag 1949, 40, 386–393.
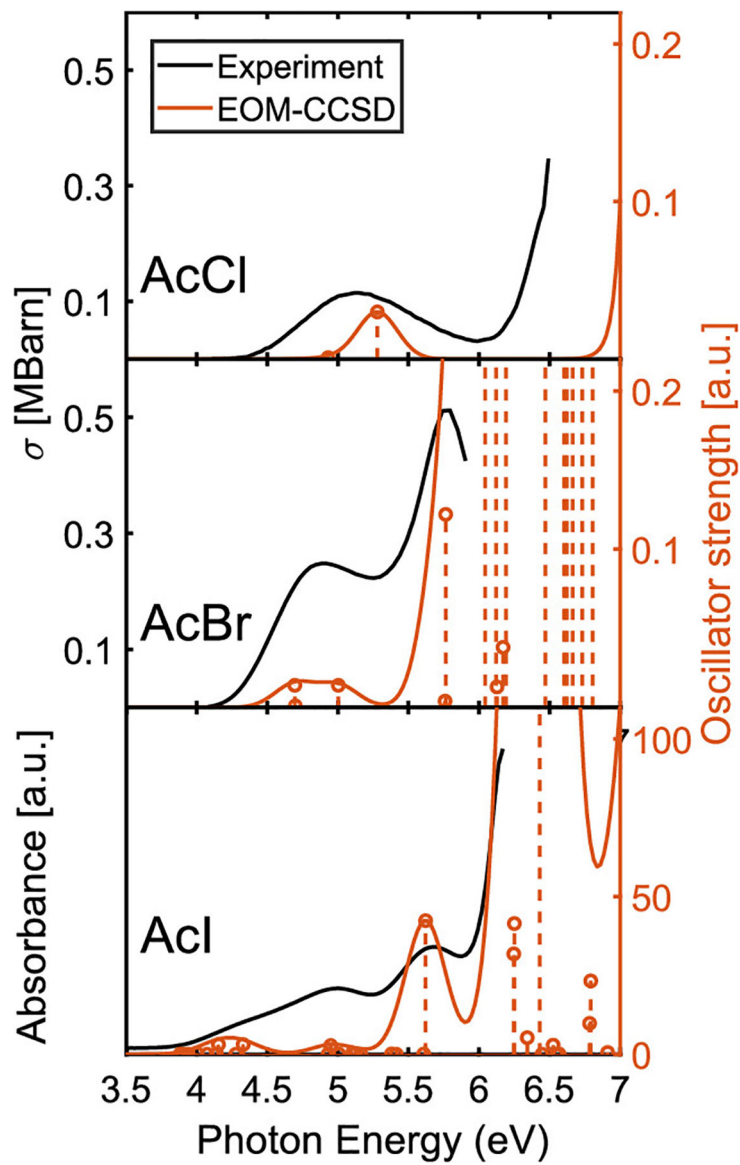
Figure 1.
Experimental and calculated UV/visible absorption spectra of gas-phase acetyl halides. Absorption cross sections of gas-phase AcCl (top panel) and AcBr (middle panel) and the absorption spectrum of AcI at 32 Torr static pressure between 3.5 and 7 eV (bottom panel). Experimental data for AcCl and AcBr are reproduced with permission from ref 108, CC BY 3.0 2013, Earth System Science Data, and ref 62, copyright 2007, Royal Society of Chemistry, respectively.
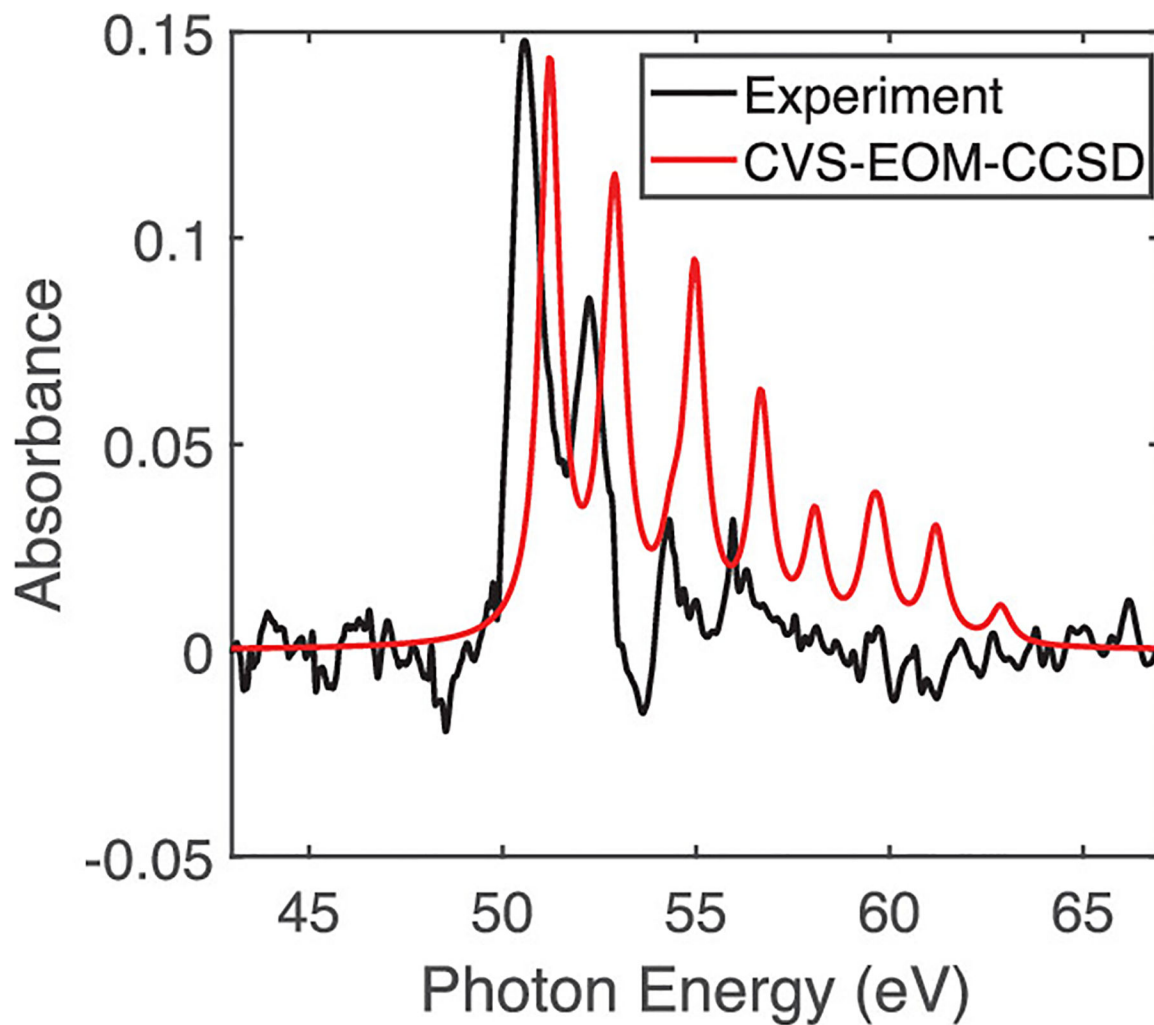
Figure 2.
XUV absorption spectrum near the iodine $N_{4,5}$ edge of gas-phase AcI at 3 Torr static pressure. The y axis is the measured optical density, defined by $OD = \log_{10}(I/I_0)$, where I and I_0 are the intensities of XUV through the interaction region with and without AcI. A broad, unstructured absorption, in excess of 0.45–0.65 OD, due to valence ionization, was subtracted from the experiment. The raw experimental spectrum is shown in Figure S2.
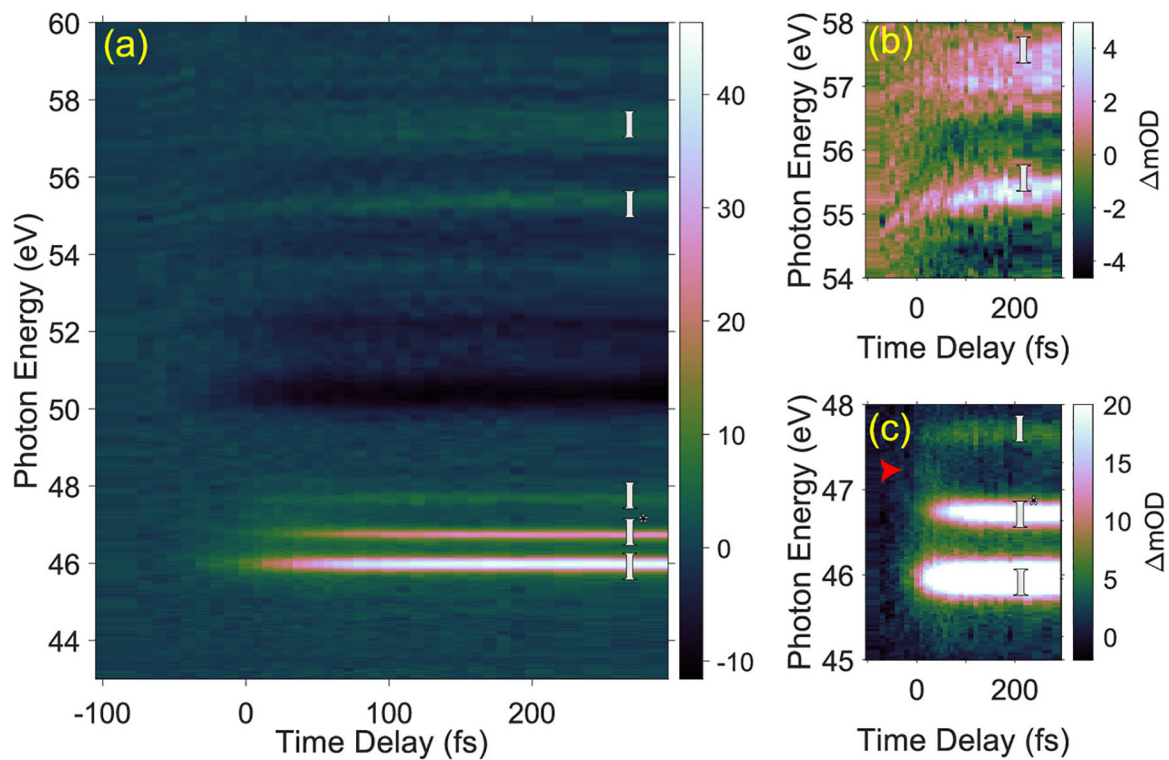
Figure 3.
Experimental time-resolved XUV absorption spectra. (a) Time-dependent differential XUV absorption, energy resolved between 43 and 60 eV. Strong bleach features between 50 and 53 eV associated with ground-state acetyl iodide are observed, and sharp induced absorption features due to atomic resonances of free iodine are detected. Time-dependent signatures associated with regions of high interest from 45 to 48 eV and from 54 to 58 eV are shown in panels (b) and (c). (b) Induced absorption between 55.1 and 55.6 eV shifts its center photon energy from 55.3 to 55.5 eV in the first 150 fs after t_0. (c) A weak short-lived signal at 47.1 eV is marked with a red arrow. An alternative color figure is given in Figure S4 in the SI.
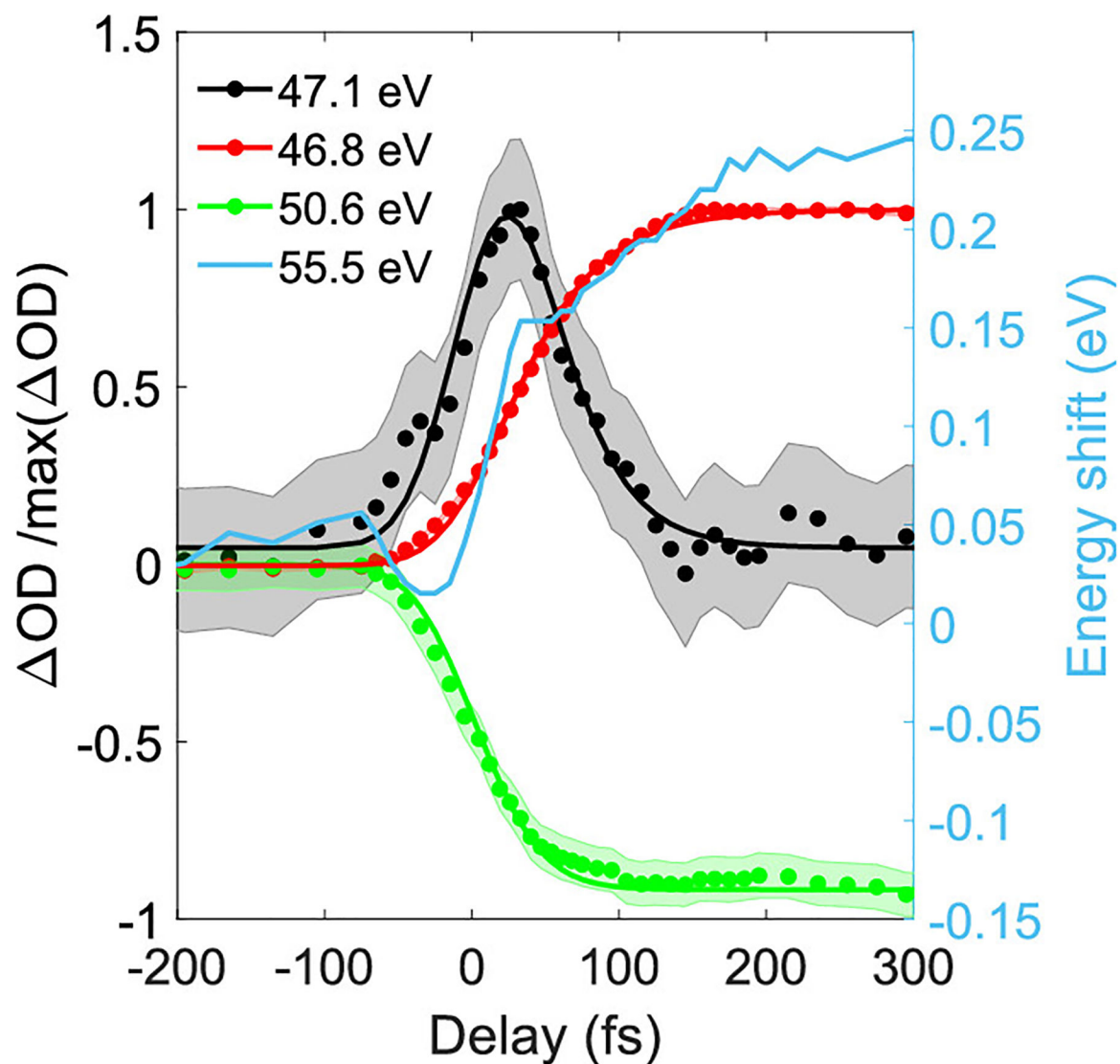
Figure 4.
Integrated differential absorbance of individual absorption features, divided by their maximum or minimum, shown as filled circles. Furthermore, a step function has been subtracted from the 47.1 eV outline, as indicated in the text. The shaded region corresponds to the $\pm 1\sigma$ error bar. Fits to these time traces are shown in color-matched solid lines. The energy shift of the 55.5 eV feature is shown in light blue.
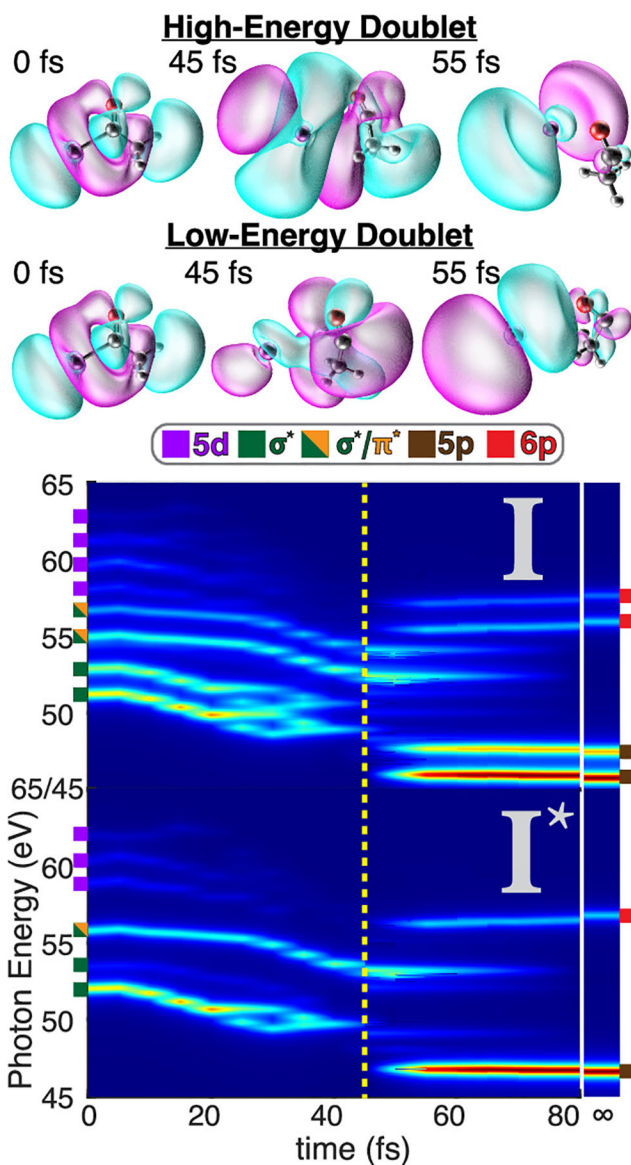
Figure 5.

False color map of the CVS-EOM-CCSD $N_{4,5}$-edge spectrum along the nonadiabatic *ai*MD trajectory taken in 5 fs increments. The I ($^2P_{3/2}$) and spin–orbit excited I* ($^2P_{1/2}$) excitation channels are shown in the top and bottom spectra, respectively. Colored notches on the left and right sides indicate the transitions ($4d{\rightarrow}A$, where $A = 5d$, σ^*, σ^*/π^*, $5p$, or $6p$) that give rise to the features at $t = 0$ and 80 fs, respectively. The σ^* orbitals that contribute to the four lowest-energy features in the AcI ($^2P_{3/2}$) spectrum are shown above the false color map. The initial σ^* orbital (left) becomes distorted as the C–I bond breaks, yielding σ^*-like orbitals that still exhibit significant hybridization between I and C_2H_3O fragments at $t = 45$ fs (center) just prior to bond breaking. After bond breaking (right), the primary transitions take on the character of pure iodine p orbitals. The spectrum of the iodine atom is shown after the break in the x axis as an approximation for $t = \infty$ to allow comparison to the finite-time spectra.